

High-order van Hove singularities and nematic instability in the kagome superconductor CsTi_3Bi_5

Bikash Patra,¹ Amrita Mukherjee,¹ and Bahadur Singh^{1,*}

¹*Department of Condensed Matter Physics and Materials Science,
Tata Institute of Fundamental Research, Mumbai 400005, India*

ATi_3Bi_5 ($A = \text{Cs}$ or Rb) are emerging topological kagome metals that exhibit superconductivity and nematicity without intertwining translational symmetry-breaking charge orders. In this work, we explore the fermiology of their titanium kagome electrons and identify a set of sublattice-pure, high-order van Hove singularities (VHSs) that can suppress charge ordering and enhance electronic correlations and superconductivity. Our calculations of charge susceptibility for kagome bands with both normal and high-order VHSs emphasize the role of these VHSs in driving electronic nematicity in CsTi_3Bi_5 . Additionally, we compute the phonon spectrum and electron-phonon interactions for CsTi_3Bi_5 under pristine, doped, and kagome-exposed surface conditions, revealing its robustness against structural instabilities while enhancing the superconducting transition temperature. Our work positions ATi_3Bi_5 as a key platform for investigating superconductivity and electronic nematicity without translational symmetry-breaking states in kagome metals.

I. INTRODUCTION

Kagome materials, with uniformly interlocked hexagonal and triangular atomic networks, provide a fundamental platform for studying the interplay between frustrated geometry, non-trivial topology, and electronic correlations [1, 2]. Their kagome lattice results in Dirac cones that encode non-trivial topology, and van Hove singularities (VHSs) and flat bands, which drive electronic correlations. These electronic features have been observed in various kagome materials, such as the presence of Weyl fermions in the ferromagnet $\text{Co}_3\text{Sn}_2\text{S}_2$ [3, 4], chiral spin textures and a significant anomalous Hall effect in the non-collinear antiferromagnet Mn_3X ($X = \text{Sn}$ and Ge) [5, 6], Dirac fermions and flat bands in FeSn and CoSn [7, 8], coexisting magnetism and superconductivity in Cu_3Sn_2 [9], and charge-density-wave (CDW) in antiferromagnetic FeGe [10].

The vanadium-based nonmagnetic kagome superconductors AV_3Sb_5 ($A = \text{K}$, Rb , or Cs) have realized a wide range of correlated states, including CDW [11–14], chiral excitonic order [15], pair density wave [16, 17], superconductivity [18, 19], and nematic order [20], often found in high-temperature superconductors [21]. The interplay between non-trivial topology and the correlated states in these materials has led to time-reversal symmetry-breaking phenomena [22, 23] and the potential emergence of Majorana zero modes [24]. Despite the diversity of quantum states in AV_3Sb_5 , the mechanisms driving these states remain unresolved. This is due in part to the complex interplay of electronic and lattice degrees of freedom, both of which can drive the system into low-energy ordered states. In AV_3Sb_5 , multiple VHSs near the Fermi level, arising from kagome electrons, create an environment prone to electronic instabilities, while the presence of soft phonon modes points to structural instabilities.

For instance, the CDW order may result from electronic nesting at the VHSs or through electron-phonon interactions. Similarly, nematic order, which breaks rotational symmetry, might arise from electronic instabilities or as a result of translational symmetry breaking associated with CDW formation. In addition, materials with HfFe_6Ge_6 -type double-kagome lattice have been identified as a promising system to study the interplay between CDW and other electronic orders, as these materials exhibit not only CDW [25–29] but also nematicity [30], magnetism [31, 32], topological properties [33, 34] and superconductivity [35]. One notable example, ScV_6Sn_6 , demonstrates the coexistence of CDW and nematicity, with the CDW primarily attributed to the Sc and Sn atoms, while the nematic order is largely associated with the kagome lattice. Despite exhibiting a $\sqrt{3} \times \sqrt{3}$ charge order, ScV_6Sn_6 maintains intra-unit-cell nematic order, preserving translational symmetry [30]. Given these complexities, recent research has increasingly focused on exploring alternative kagome materials that are devoid of instabilities stemming from both electronic and phonon degrees of freedom.

Recently, kagome materials based on titanium atomic networks, ATi_3Bi_5 ($A = \text{Rb}$ or Cs), isostructural to AV_3Sb_5 with Ti and Bi atoms substituting V and Sb , have gained attention [36–42]. Spectroscopic studies on ATi_3Bi_5 revealed canonical kagome electronic features, including a flat band, VHSs, and Dirac nodal lines from kagome bands crossing with trivial bands [38–40]. The superconducting state of these materials remains contentious, with some reports suggesting a superconducting transition temperature (T_c) close to 4.8 K, while others found no superconductivity at ambient conditions [43–45]. First-principles calculations predict that ATi_3Bi_5 falls within the low electron-phonon coupling regime at the Fermi filling, with a calculated T_c of 0.13 K [46]. Notably, transport experiments reveal no CDW anomalies in contrast to AV_3Sb_5 . However, ATi_3Bi_5 exhibits direction-dependent scattering wave vectors [39–41], in-

* bahadur.singh@tifr.res.in

dicating a multi-orbital Fermi surface and the emergence of a pure electronic nematic phase, akin to those in high-temperature superconductors [47, 48]. These findings call for detailed investigations of electronic structure and electron-phonon interactions in ATi_3Bi_5 to clarify the role of electronic and phonon degrees of freedom in the formation of the various quantum states.

In this paper, we provide a comprehensive analysis of the electronic structure and electron-phonon interactions in CsTi_3Bi_5 using a uniform first-principles framework. We elucidate the multi-orbital nature of the Fermi surface, highlighting contributions from both Ti d and Bi p states, which hybridize to form multi-orbital Fermi pockets. The kagome bands near the Fermi level arise from Ti $d_{x^2-y^2}/d_{xy}$ states, with flat bands situated below the Fermi level, while VHSs and Dirac bands appear above it. Notably, both the VHSs are high-order and sublattice-pure, differing from those in AV_3Sb_5 . Our detailed charge susceptibility calculations indicate that these high-order VHSs reduce Fermi surface nesting and can drive electronic instabilities. We also demonstrate the stability of CsTi_3Bi_5 against soft phonon modes and translational symmetry-breaking through analyses of phonon dispersions of pristine, charge-doped, and kagome-exposed surface conditions. Additionally, we explore strategies to enhance the superconducting T_c by tuning the Fermi level to align with flat bands or VHSs via hole and electron doping. Our results highlight that CsTi_3Bi_5 is a unique kagome material that possesses the necessary properties for realizing electronic instabilities such as nematicity and superconductivity, consistent with experimental findings.

II. METHODOLOGY

Electronic structure calculations were performed within the density functional theory framework with projector-augmented wave potentials [49, 50], using the Vienna ab initio simulation package (VASP) [51, 52]. The Perdew-Burke-Ernzerhof (PBE) parameterization of the generalized gradient approximation (GGA) was employed to consider exchange-correlation effects [53]. An energy cutoff of 330 eV was set for the plane wave basis set, and a $10 \times 10 \times 8$ Γ -centered k -point mesh was used for Brillouin zone sampling. Lattice parameters and ionic positions were optimized until the residual forces on each ion were less than 1.0×10^{-3} eV/atom. The optimized structural parameters are given in Table I. We constructed a material-specific tight-binding model Hamiltonian from atom-centered Wannier functions, considering Ti s , d , and Bi p states [54]. Finer k -mesh electronic structure calculations and charge-susceptibility analyses were performed using the obtained tight-binding Hamiltonian of CsTi_3Bi_5 .

The superconducting T_c of CsTi_3Bi_5 was obtained by evaluating the electron-phonon interaction based on the Eliashberg spectral function ($\alpha^2F(\omega)$) with Quantum

ESPRESSO (QE) [55] and EPW [56] codes. The energy spectrum in QE was calculated with PBE-GGA density functional and norm-conserving PBE pseudopotentials with standard accuracy from the PseudoDojo library [57] using the relaxed parameters obtained in VASP. A plane-wave energy cutoff of 60 Ry and a charge density cutoff of 480 Ry were used. The phonon spectrum was obtained through density functional perturbation theory. Notably, we confirmed the consistency of the electron and phonon dispersions calculated in VASP and QE codes and found a good agreement between them (see the Supplemental Materials (SM)) [58]. For electron-phonon coupling, a carefully converged fine $32 \times 32 \times 24$ k -grid and $16 \times 16 \times 12$ q -grid were used in the bulk Brillouin zone [58]. The effects of additional carriers in CsTi_3Bi_5 were simulated by adding and removing electrons in the unit cell with a neutralizing uniform background charge. For the calculation of susceptibilities, a fine 200×200 k mesh was used at temperature $T = 0.01$ K.

III. RESULTS AND DISCUSSION

A. Crystal structure and electronic state

CsTi_3Bi_5 forms a layered hexagonal crystal structure with the space group $P6/mmm$ (No. 191) [Fig. 1(a)]. In this structure, the Cs and Ti atoms occupy the Wyckoff positions $1a$ (0, 0, 0) and $3g$ ($\frac{1}{2}, \frac{1}{2}, \frac{1}{2}$), respectively, while two types of Bi atoms are located at the Wyckoff positions $4h$ ($\frac{1}{3}, \frac{2}{3}, 0.2387$) and $1b$ (0, 0, $\frac{1}{2}$). The structure features a two-dimensional (2D) Ti kagome lattice, with Bi atoms filling the hexagonal centers. This interlaced kagome-Bi lattice is sandwiched between two Bi honeycomb layers that are weakly bonded to the kagome lattice. The Cs atoms form a triangular layer situated between the kagome layers. Table I presents the optimized lattice parameters of CsTi_3Bi_5 obtained using various exchange-correlation functionals. The lattice parameters calculated with the PBE functional are overestimated, particularly the c parameter, which exceeds the experimental value by $\sim 8.9\%$. Incorporating van der Waals (vdW) interactions during geometry optimization

TABLE I. Calculated lattice parameters for CsTi_3Bi_5 using different exchange-correlation functionals. a and c represent in-plane and out-of-plane lattice constants, respectively. $d_{\text{Ti-Bi}}^{\parallel}$ and $d_{\text{Ti-Bi}}^{\perp}$ denote the in-plane and out-of-plane interatomic distance between Ti and Bi atoms.

| | a (\AA) | c (\AA) | $d_{\text{Ti-Bi}}^{\parallel}$ (\AA) | $d_{\text{Ti-Bi}}^{\perp}$ (\AA) |
|-----------|----------------------|----------------------|---|---|
| PBE | 5.803 | 10.027 | 2.901 | 2.974 |
| PBE+vdW | 5.745 | 9.482 | 2.873 | 2.957 |
| SCAN | 5.759 | 9.656 | 2.879 | 2.938 |
| R2SCAN | 5.785 | 9.787 | 2.892 | 2.953 |
| SCAN+vdW | 5.752 | 9.435 | 2.876 | 2.934 |
| Exp. [36] | 5.787 | 9.206 | 2.893 | 2.929 |

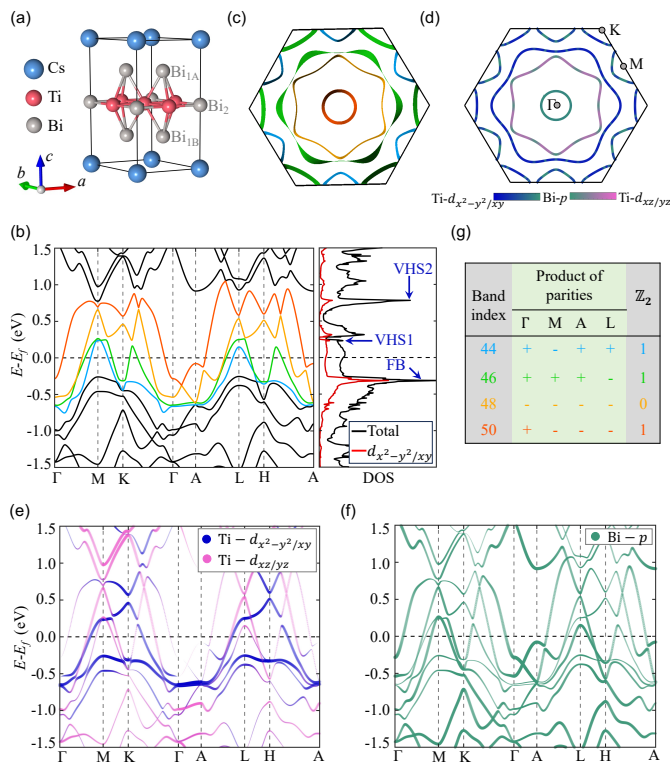


FIG. 1. (a) Crystal structure of CsTi_3Bi_5 with Ti kagome net (indicated in red). Bi_{1A} and Bi_{2B} represent two honeycomb Bi layers within the lattice. (b) Electronic structure of CsTi_3Bi_5 with spin-orbit coupling. Blue arrows in the density of states (DOS) highlight saddle-point van Hove singularities (VHS1 and VHS2) and flat band (FB) associated with Ti kagome electrons. (c) Top view of the Fermi surface and (d) orbital-resolved Fermi band contours at the $k_z = 0$ plane of CsTi_3Bi_5 . Two-dimensional Fermi pockets with multi-orbital contributions are evident. (e)-(f) Orbital-resolved band structures of CsTi_3Bi_5 with (e) Ti and (f) Bi states. Symbol size is proportional to the orbital weight. (g) Parity products at time-reversal invariant momentum points and the associated \mathbb{Z}_2 invariant for CsTi_3Bi_5 .

with PBE reduces the deviation from experimental values. The more advanced SCAN meta-GGA functional, when combined with vdW interactions, yields lattice parameters that closely align with experimental data. Since the lattice parameters derived from PBE and SCAN with vdW interactions differ only slightly, we employ the PBE+vdW optimized parameters to describe the electronic and phononic properties of CsTi_3Bi_5 in the following discussion.

Figure 1(b) presents the electronic structure of CsTi_3Bi_5 with spin-orbit coupling. The band structure features four dispersive band crossings at the Fermi level with similar characteristics at the $k_z = 0$ and $k_z = \pi/c$ planes, which highlights the strong 2D nature of the Fermi pockets (Fig. 1(c)). Despite its complexity, key Kagome features are apparent in the orbital-resolved band structure and partial density of states (Figs. 1(b)

and 1(e)). The kagome bands are predominantly composed of Ti $d_{x^2-y^2}/d_{xy}$ orbitals with the saddle-point VHSs (VHS1 and VHS2) and Dirac points located above the Fermi level and flat bands below it. The Dirac points at the K and H points exhibit small gaps due to spin-orbit coupling. Notably, the VHSs and Dirac points in CsTi_3Bi_5 are located above the Fermi level, in contrast to those in AV_3Sb_5 materials, due to the one-electron deficiency of Ti compared to V. The position of the flat bands below the Fermi level is ascertained by the orbitals contributing to the kagome bands [59]. When the kagome bands are formed by d_{xz}/d_{yz} orbitals, the flat band lies above the Dirac point. However, when the bands consist primarily of $d_{x^2-y^2}/d_{xy}$ orbitals, a sign change in the off-diagonal matrix elements shifts the flat band below the Dirac point, as seen in CsTi_3Bi_5 .

Figure 1(c) illustrates the top view of the Fermi surface, comprising five 2D Fermi pockets: three centered at the Γ point (one circular, one hexagonal, and one snowflake), one diamond-like pocket at the M point, and one triangular pocket at the K point. These pockets exhibit substantial hybridization between Ti d and Bi p bands, with varying character across the Fermi surface, as shown in the orbital-resolved Fermi band contours in Fig. 1(d). The central circular pocket is derived from Bi p orbitals, while the snowflake pocket is primarily contributed by Ti $d_{x^2-y^2}/d_{xy}$ orbitals that form kagome bands. The remaining three pockets demonstrate strong $d-p$ hybridization, with their character alternating across the Fermi surface, resolving a momentum-dependent hybridization (see Figs. 1(d)-1(f)). This multi-orbital Fermi surface is similar to that of the FeSe superconductor, which also exhibits nematic instability. These Fermi surface characteristics are consistent with ARPES studies of CsTi_3Bi_5 , which demonstrate polarization-selective band structure [40].

We emphasize that, despite the metallic nature of CsTi_3Bi_5 , the band structure exhibits a local energy gap at all time-reversal invariant momentum points. These energy gaps enable the calculations of the \mathbb{Z}_2 invariant using the parity criterion [60]. Figure 1(g) presents the product of occupied band parities at various momentum points, along with the calculated nontrivial \mathbb{Z}_2 invariant. These results indicate that CsTi_3Bi_5 can host topological surface states within the local energy gaps, as reported in experimental studies [38, 40].

B. VHSs and nematic instability

We now examine the kagome electronic features and their role in driving electronic nematic order in CsTi_3Bi_5 . Figure 2(a) presents the Ti $d_{x^2-y^2}/d_{xy}$ orbital-resolved band structure, highlighting the Kagome electronic features near the Fermi level. The two VHSs, VHS1 and VHS2, are located at energies 0.22 eV and 0.74 eV above the Fermi level at M point, respectively, while a flat band lies around -0.4 eV below it. These kagome bands cross

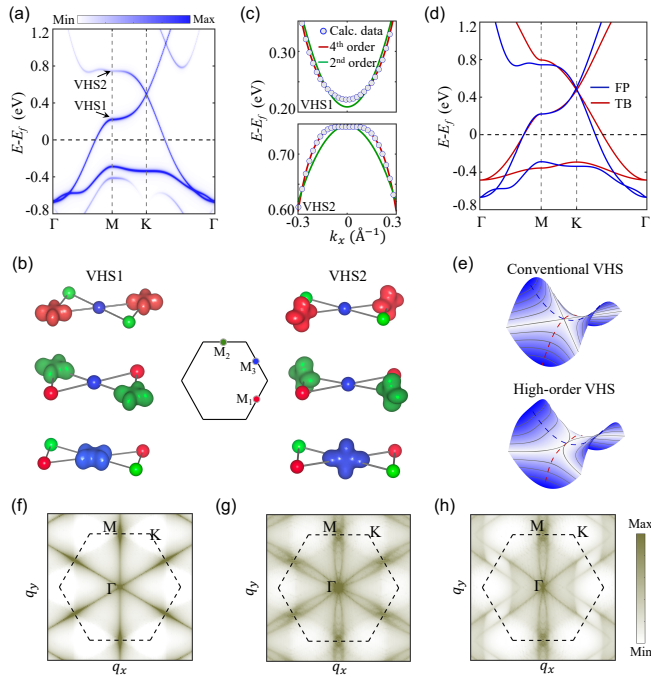


FIG. 2. (a) Orbital-projected band structure for Ti $d_{x^2-y^2}/d_{xy}$ states of CsTi₃Bi₅ at the $k_z = 0$ plane, highlighting distinct electronic features of the Ti kagome lattice. (b) Charge density profiles of Bloch wave functions for saddle-point van Hove singularities, VHS1 and VHS2, at three equivalent M points in the Brillouin zone. (c) Energy dispersion along k_x at VHSs, with second and fourth-order polynomial fittings. (d) Calculated band structure of the kagome lattice using the tight-binding model (TB), incorporating nearest and next-nearest neighbor interactions along with first-principles (FP) results. (e) Schematic representation of conventional and high-order VHSs, with grey curves denoting the constant energy contours. (f)-(h) Calculated momentum distribution of bare charge susceptibility $\chi(\mathbf{q})$ for (f) normal VHS (g) high-order VHS derived from CsTi₃Bi₅ band fittings. (h) Charge susceptibility for high-order VHS by varying onsite energy of one of the kagome sublattices (see text for details).

the Fermi level, forming the Dirac cone at the K point. To characterize the flavor of VHSs, we isolate the sublattice projections of the Bloch wave functions at VHSs, as shown in Fig. 2(b). Both VHS1 and VHS2 are sublattice pure, with each sublattice contributing VHS at different M points. Typically, in a kagome band structure, two VHSs exhibit a mix of sublattice pure and mixed characters; however, both VHSs here are sublattice pure without exhibiting mixed characters. This behavior arises from the three-dimensionality of VHS2, resulting from the mixing of Ti $d_{x^2-y^2}/d_{xy}$ with Ti d_{z^2} orbitals. The sublattice-pure decoration of VHSs splits the three prominent particle-hole scattering channels in the hexagonal Fermi surface into six, thereby weakening the instabilities like CDW while promoting sublattice interference and long-range interactions [61] (see SM of additional details) [58].

To analyze the order of VHSs [62], we fit the energy dispersion around the saddle points (VHS1 and VHS2) along the $M-K-M$ direction using both quadratic and quartic polynomials, as shown in Fig. 2(c). The band dispersion is better described by a quartic polynomial $E = a + bk_x^2 + ck_x^4$, with fitting parameters $a = 0.22$, $b = 1.07$, and $c = 7.63$ for VHS1, and $a = 0.74$, $b = -0.33$, and $c = -13.87$ for VHS2. The goodness-of-fit parameters, R-square and root mean square error (RMSE), are 0.9999 and 0.0014 for VHS1 and 0.9988 and 0.0003 for VHS2. These values, with R-squared close to 1 and RMSE near 0, confirm the excellent quality of the quartic polynomial fit. The deviation of energy dispersion from a normal quadratic form indicates the presence of high-order VHSs (Fig. 2(e)). The high-order VHSs warp the ideal hexagonal Fermi surface associated with normal VHSs, reducing Fermi surface nesting and associated instabilities. Simultaneously, they enhance the DOS, thereby amplifying correlations-driven many-body effects. The sublattice-pure high-order VHSs in CsTi₃Bi₅ thus suggest a decreased likelihood of CDW instabilities while enhancing sublattice interference and electron correlation effects [63–65]. This interplay can ultimately strengthen electronic instabilities. Such phenomena have been observed in materials like CsV₃Sb₅ [66] and high T_c cuprates [67], where significant many-body effects prevail.

We now explore how sublattice-pure high-order VHSs weaken CDW instabilities by employing a tight-binding Hamiltonian for kagome bands,

$$H = t \sum_{\langle i,j \rangle} c_i^\dagger c_j + t' \sum_{\langle\langle i,j \rangle\rangle} c_i^\dagger c_j + H.c. \quad (1)$$

where t , and t' are the nearest-neighbour and next-nearest-neighbour hopping parameters, respectively. The energy dispersion for $t = 0.35$ and $t' = 0.035$ is shown in Fig. 2(d). These parameters accurately reproduce the bands at VHS1 but show significant deviations at the VHS2, likely due to contributions from other orbitals and the interference between in-plane and out-of-plane d orbital hoppings. At VHS1, we calculate the bare charge susceptibility $\chi(\mathbf{q})$ using the constant matrix approximation,

$$\chi(\mathbf{q}) = - \sum_{\mathbf{k}, m, n} \frac{f(\epsilon_{n\mathbf{k}}) - f(\epsilon_{m\mathbf{k}+\mathbf{q}})}{\epsilon_{n\mathbf{k}} - \epsilon_{m\mathbf{k}+\mathbf{q}} + i\Gamma} \quad (2)$$

where $\epsilon_{m/n,\mathbf{k}}$ is the eigenvalue of band m/n at \mathbf{k} , $f(\epsilon)$ is the Fermi-Dirac distribution, and \mathbf{q} is the nesting vector. The susceptibility $\chi(\mathbf{q})$ at normal VHS of a kagome lattice with $t' = 0$, shown in Fig. 2(f), exhibit high intensity along the $\Gamma - M$ lines with peak at the M points. This indicates strong particle-hole scattering linked by nesting vectors $\mathbf{q} = \{(0, \pi), (\pi, 0), (-\pi, \pi)\}$, suggesting formation of potential 2×2 CDW order. However, warped hexagonal Fermi surface due to high-order VHS1 reduces the divergence in $\chi(\mathbf{q})$ at M points (see Fig. 2(g)). This reduction can be further diminished by considering sublattice

decoration to the Fermi surface that modifies the scattering channels, indicating a lower probability of CDW instability.

The aforementioned discussion indicates the possibility of electronic nematic instability in CsTi_3Bi_5 , as observed in scanning tunneling microscopy measurements [39]. Notably, the nematic order in CsTi_3Bi_5 reduces the C_6 rotation symmetry to C_2 symmetry. Due to the sublattice pure VHSs, a simple onsite potential can break rotation symmetry, distorting the Fermi surface and lowering the density of states at VHSs [30]. To test this phenomenology, we introduce an onsite potential in one of the sublattices, which effectively modifies the states in one of the three inequivalent M points. The resulting $\chi(\mathbf{q})$, shown in Fig. 2(h), demonstrates that the C_6 symmetry of the system is broken, leading to the emergence of C_2 symmetry. While this model captures the symmetry lowering in the absence of CDW ordering, the multi-orbital Fermi surface and sublattice interference result in non-uniform symmetry breaking, as seen in quasiparticle interference patterns, which warrant further investigation [39–41].

C. Robustness of structural stability

We now examine the possibility of lattice instabilities in CsTi_3Bi_5 . While the VHSs suggest possible electronic instabilities, they are situated slightly above the Fermi level. Therefore, it is essential to investigate dynamical instabilities that may arise from shifting the Fermi level to the VHSs or flat band energies. Figure 3(a) shows the phonon dispersion for pristine CsTi_3Bi_5 , along with its electron and hole doping cases. In all cases, the phonon eigenvalues remain positive without any imaginary values across the full Brillouin zone. There are only minor changes in the phonon bands even under substantial doping of 1 electron (hole) per unit cell, which moves the Fermi level to the VHS1 (near flat band) energies (see SM) [58]. We also assessed the lattice stability by applying 1% compressive and tensile strains (Fig. 3(b)), which similarly yield stable phonon modes. The absence of imaginary phonon frequencies under various conditions suggests that CsTi_3Bi_5 is robust against lattice instabilities. Notably, even moving the Fermi level to the VHSs or flat bands through doping has no detrimental impact on lattice stability. These results align well with recent experimental reports indicating that CsTi_3Bi_5 exhibits no structural instabilities even when the VHSs are moved to the Fermi level through Cs doping [42].

In bulk kagome materials, the kagome atomic layers are typically buried deep within the structure, complicating the assessment of their influence on structural instabilities. To examine the role of the Ti kagome layer, we calculated the surface phonon dispersions of CsTi_3Bi_5 for two surface terminations: one that directly exposes the Ti kagome layer and another that positions it just beneath the surface. The phonon spectra for both termi-

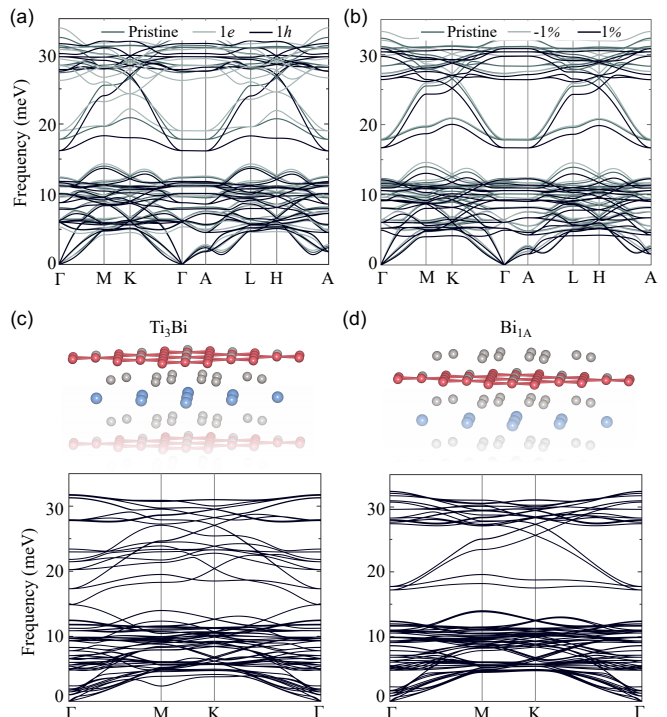


FIG. 3. (a) Phonon spectrum of CsTi_3Bi_5 for pristine, electron-doped, and hole-doped phases. (b) Phonon spectrum of CsTi_3Bi_5 for pristine phase and under compressive and tensile strains. (c)-(d) Phonon spectrum of CsTi_3Bi_5 slab with (c) Ti_3Bi surface termination exposing the Ti-kagome layer and (d) Bi_{1A} honeycomb layer termination. No imaginary phonon frequencies are evident under these conditions.

nations, presented in Figs. 3(c) and 3(d), reveal no imaginary phonon frequencies in the surface Brillouin zone. These results indicate that CsTi_3Bi_5 retains structural stability even with the kagome layer is exposed at the surface, suggesting that any potential instabilities here would be driven by electronic factors. These characteristics position CsTi_3Bi_5 as a unique kagome system, especially in contrast to isostructural AV_3Sb_5 materials and bi-kagome layer systems such as AV_6Sn_6 , which exhibit significant lattice instabilities in their surface-exposed kagome layers [68].

D. Filling dependent electron-phonon interaction and superconductivity

After confirming that CsTi_3Bi_5 is stable against lattice instabilities, we now explore the possibility of superconductivity in both pristine and doped conditions (electron and hole doping). In Fig. 4(a), we present phonon spectrum weighted by wave-vector resolved electron-phonon coupling $\lambda_{\nu\mathbf{q}}$, along with Eliashberg spectral function $\alpha^2F(\omega)$ and the cumulative electron-phonon coupling λ at the charge neutrality point. The Eliashberg spectral

function is defined as

$$\alpha^2 F(\omega) = \frac{1}{N_f N_{\mathbf{k}} N_{\mathbf{q}}} \sum_{n\mathbf{k}, m\mathbf{k}', \nu} |g_{n\mathbf{k}, m\mathbf{k}'}^\nu|^2 \delta(\epsilon_{n\mathbf{k}}) \delta(\epsilon_{m\mathbf{k}'}) \delta(\omega - \omega_{\nu\mathbf{q}}) \quad (3)$$

where N_f represents the density of states at the Fermi level ϵ_f , $N_{\mathbf{k}}$ and $N_{\mathbf{q}}$ denote the number of \mathbf{k} and \mathbf{q} points. $\epsilon_{n\mathbf{k}}$ and $\omega_{\nu\mathbf{q}}$ give the electronic and phononic eigenvalues and $g_{n\mathbf{k}, m\mathbf{k}'}^\nu$ corresponds to the electron-phonon matrix element. The cumulative electron-phonon coupling λ and wave-vector resolved electron-phonon coupling $\lambda_{\nu\mathbf{q}}$ are given by

$$\lambda = \sum_{\nu\mathbf{q}} \lambda_{\nu\mathbf{q}} = 2 \int \frac{\alpha^2 F(\omega)}{\omega} d\omega \quad (4)$$

The Eliashberg spectral function in Fig. 4(a) reveals four prominent peaks: one in the low-frequency region and the other three in the high-frequency region. This gives a cumulative electron-phonon coupling strength $\lambda = 0.33$, indicating a low electron-phonon coupling regime of CsTi₃Bi₅. While all phonon bands contribute to the total electron-phonon coupling, the contribution of each mode varies significantly. The low-frequency modes account for $\sim 68\%$ of the total electron-phonon coupling (Fig 4(a)). The distribution of $\lambda_{\nu\mathbf{q}}$ in the $k_z = 0$ plane is shown in Fig 4(b), which reveals substantial variation of $\lambda_{\nu\mathbf{q}}$ in the entire plane. The associated superconducting critical temperature T_c , calculated using the modified McMillan formula [69],

$$T_c = \frac{\omega_{log}}{1.2} \exp \left[\frac{-1.04(1 + \lambda)}{\lambda - \mu^*(1 + 0.62\lambda)} \right] \quad (5)$$

where μ^* is the effective screened Coulomb repulsion, and $\omega_{log} = \exp \left[\frac{2}{\lambda} \int \frac{\alpha^2 F(\omega)}{\omega} \log(\omega) d\omega \right]$ is the logarithmically averaged phonon frequency, yields $T_c \sim 0.13$ K for $\mu^* = 0.10$. This very low value of T_c at the charge neutrality point is consistent with experimental results of minimal or absent superconductivity.

Next, we evaluate the electron-phonon coupling and superconducting T_c under electron doping (1 electron/unit cell), which shifts the Fermi level to VHS1. The band-resolved $\lambda_{\nu\mathbf{q}}$ now spans the entire frequency spectrum while still maintaining its maximum in the low-frequency range (Fig. 4(c)). This is also reflected in the Eliashberg spectral function, which shows an enhanced peak in the high-frequency region. The high-frequency phonon modes contribute $\sim 38\%$ of the total electron-phonon coupling, an increase of 6% compared to the charge-neutral case. In Fig. 4(d), we illustrate the momentum-resolved electron-phonon coupling on the $k_z = 0$ plane, where the dominant contribution is still centered around Γ , with additional enhancement near the M points. The calculated T_c rises to 5.66 K. When the Fermi level is tuned to the flat bands by removing two electrons per unit cell (hole doping), λ increases to 1.12, resulting in a T_c enhancement to 13.3 K-over 10 times greater than at the charge neutrality point. Such enhancement is expected, as flat bands are known to

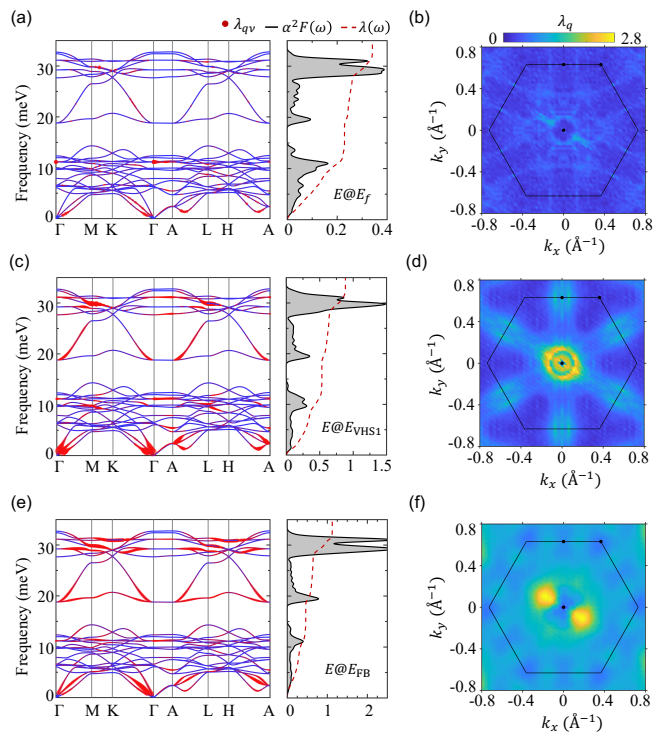


FIG. 4. (a) Phonon dispersion, Eliashberg spectral function $\alpha^2 F(\omega)$ and accumulated electron-phonon coupling constant $\lambda(\omega)$; and (b) distribution of the electron-phonon coupling strength $\lambda_{\nu\mathbf{q}}$ at $k_z = 0 \text{ \AA}^{-1}$ plane for CsTi₃Bi₅ at the charge neutral point. The size of red markers in the phonon spectrum is proportional to the band-resolved electron-phonon coupling strength $\lambda_{\nu\mathbf{q}}$. (c)-(d) and (e)-(f) present the same data as (a)-(b), but obtained for (c)-(d) at VHS filling (electron doping) and (e)-(f) at flat band filling (hole doping). An enhancement of electron-phonon coupling is evident at both VHS and flat band fillings.

strengthen electron-phonon coupling and superconducting T_c . Given that CsTi₃Bi₅ is susceptible to charge doping with a tunable band structure [42], enhanced superconductivity can be achieved by moving away from the charge neutrality point through both electron and hole doping.

IV. SUMMARY

We provide the first comprehensive description of the electronic structure and dynamical properties of CsTi₃Bi₅ through first-principles theoretical modeling. Our analysis reveals the nature of Ti kagome electrons and their role in driving electronic instabilities in CsTi₃Bi₅. We demonstrate that the Fermi surface exhibits a multi-orbital character, with contributions from both Ti d and Bi p states, which are hybridized throughout the Brillouin zone. The kagome bands near the Fermi level primarily originate from the Ti- $d_{x^2-y^2}/d_{xy}$ bands and support sublattice pure and high-order VHSs that

enhance sublattice interference and long-range electron correlations while reducing Fermi surface nesting. Based on the bare charge susceptibility associated with electrons near the normal and high-order VHSs, we compare and contrast the reduction in particle-hole scattering and demonstrate the emergence of electronic nematic order, characterized by the lowering of C_6 rotational symmetry to C_2 . Our phonon dispersions of pristine, doped, strained, and kagome-layer-exposed surface conditions demonstrate that CsTi_3Bi_5 is stable against lattice distortions and CDW instabilities. We also explore the enhancement of superconductivity by shifting the Fermi level away from the charge neutrality point, demonstrating a tenfold increase in T_c as the Fermi level approaches the flat band energies. While kagome materials are well known for supporting many-body instabilities, discerning

their origins remain challenging. Our results here position CsTi_3Bi_5 as a unique kagome metal where Fermi surface nesting and soft phonon modes driven CDW instabilities are absent. Instead, the presence of sublattice-pure high-order VHSs and the multi-orbital nature of the Fermi surface clearly signal the presence of electronic instabilities, such as nematicity and superconductivity in agreement with experimental results.

ACKNOWLEDGEMENTS

We thank S. Mardanya for helpful discussions on susceptibility calculations. This work is supported by the Department of Atomic Energy of the Government of India under Project No. 12-R&D-TFR-5.10-0100 and benefited from the computational resources of TIFR Mumbai.

-
- [1] I. Syőzi, Statistics of Kagomé Lattice, *Prog. Theor. Phys.* **6**, 306 (1951).
- [2] Y. Wang, H. Wu, G. T. McCandless, J. Y. Chan, and M. N. Ali, Quantum states and intertwining phases in kagome materials, *Nat. Rev. Phys.* **5**, 635 (2023).
- [3] D. F. Liu, A. J. Liang, E. K. Liu, Q. N. Xu, Y. W. Li, C. Chen, D. Pei, W. J. Shi, S. K. Mo, P. Dudin, T. Kim, C. Cacho, G. Li, Y. Sun, L. X. Yang, Z. K. Liu, S. S. P. Parkin, C. Felser, and Y. L. Chen, Magnetic weyl semimetal phase in a kagomé crystal, *Science* **365**, 1282 (2019).
- [4] Y. Okamura, S. Minami, Y. Kato, Y. Fujishiro, Y. Kaneko, J. Ikeda, J. and Muramoto, R. Kaneko, K. Ueda, V. Kocsis, N. Kanazawa, Y. Taguchi, T. Koretsune, K. Fujiwara, A. Tsukazaki, R. Arita, Y. Tokura, and Y. Takahashi, Giant magneto-optical responses in magnetic weyl semimetal $\text{Co}_3\text{Sn}_2\text{S}_2$, *Nat. Commun.* **11**, 4619 (2020).
- [5] H. Yang, Y. Sun, Y. Zhang, W.-J. Shi, S. S. P. Parkin, and B. Yan, Topological weyl semimetals in the chiral antiferromagnetic materials Mn_3Ge and Mn_3Sn , *New J. Phys.* **19**, 015008 (2017).
- [6] T. Chen, T. Tomita, S. Minami, M. Fu, T. Koretsune, M. Kitatani, I. Muhammad, D. Nishio-Hamane, R. Ishii, F. Ishii, R. Arita, and S. Nakatsuji, Anomalous transport due to weyl fermions in the chiral antiferromagnets Mn_3X , $\text{X} = \text{Sn, Ge}$, *Nat. Commun.* **12**, 572 (2021).
- [7] M. Kang, L. Ye, S. Fang, J.-S. You, A. Levitan, M. Han, J. I. Facio, C. Jozwiak, A. Bostwick, E. Rotenberg, M. K. Chan, R. D. McDonald, D. Graf, K. Kaznatcheev, E. Vescovo, D. C. Bell, E. Kaxiras, J. van den Brink, M. Richter, M. Prasad Ghimire, J. G. Checkelsky, and R. Comin, Dirac fermions and flat bands in the ideal kagome metal FeSn , *Nat. Mater.* **19**, 163 (2020).
- [8] M. Kang, S. Fang, L. Ye, H. C. Po, J. Denlinger, C. Jozwiak, A. Bostwick, E. Rotenberg, E. Kaxiras, J. G. Checkelsky, and R. Comin, Topological flat bands in frustrated kagome lattice CoSn , *Nat. Commun.* **11**, 4004 (2020).
- [9] S. Baidya, A. V. Mallik, S. Bhattacharjee, and T. Saha-Dasgupta, Interplay of magnetism and topological superconductivity in bilayer kagome metals, *Phys. Rev. Lett.* **125**, 026401 (2020).
- [10] X. Wen, Y. Zhang, C. Li, Z. Gui, Y. Li, Y. Li, X. Wu, A. Wang, P. Yang, B. Wang, J. Cheng, Y. Wang, J. Ying, and X. Chen, Unconventional charge density wave in a kagome lattice antiferromagnet fege, *Phys. Rev. Res.* **6**, 033222 (2024).
- [11] Y.-P. Lin and R. M. Nandkishore, Complex charge density waves at van hove singularity on hexagonal lattices: Haldane-model phase diagram and potential realization in the kagome metals AV_3Sb_5 ($A = \text{K, Rb, Cs}$), *Phys. Rev. B* **104**, 045122 (2021).
- [12] H. Li, T. T. Zhang, T. Yilmaz, Y. Y. Pai, C. E. Marvinney, A. Said, Q. W. Yin, C. S. Gong, Z. J. Tu, E. Vescovo, C. S. Nelson, R. G. Moore, S. Murakami, H. C. Lei, H. N. Lee, B. J. Lawrie, and H. Miao, Observation of unconventional charge density wave without acoustic phonon anomaly in kagome superconductors AV_3Sb_5 ($A = \text{Rb, Cs}$), *Phys. Rev. X* **11**, 031050 (2021).
- [13] M. M. Denner, R. Thomale, and T. Neupert, Analysis of charge order in the kagome metal AV_3Sb_5 ($A = \text{K, Rb, Cs}$), *Phys. Rev. Lett.* **127**, 217601 (2021).
- [14] H. Tan, Y. Liu, Z. Wang, and B. Yan, Charge density waves and electronic properties of superconducting kagome metals, *Phys. Rev. Lett.* **127**, 046401 (2021).
- [15] H. D. Scammell, J. Ingham, T. Li, and O. P. Sushkov, Chiral excitonic order from twofold van hove singularities in kagome metals, *Nat. Commun.* **14**, 605 (2023).
- [16] S. Zhou and Z. Wang, Chern fermi pocket, topological pair density wave, and charge-4e and charge-6e superconductivity in kagomé superconductors, *Nat. Commun.* **13**, 7288 (2022).
- [17] H. Chen, H. Yang, B. Hu, Z. Zhao, J. Yuan, Y. Xing, G. Qian, Z. Huang, G. Li, Y. Ye, S. Ma, S. Ni, H. Zhang, Q. Yin, C. Gong, Z. Tu, H. Lei, H. Tan, S. Zhou, C. Shen, X. Dong, B. Yan, Z. Wang, and H.-J. Gao, Roton pair density wave in a strong-coupling kagome superconductor, *Nature* **599**, 222 (2021).
- [18] B. R. Ortiz, S. M. L. Teicher, Y. Hu, J. L. Zuo, P. M. Sarte, E. C. Schueller, A. M. M. Abeykoon, M. J. Krogstad, S. Rosenkranz, R. Osborn, R. Seshadri, L. Ba-

- lents, J. He, and S. D. Wilson, CsV₃Sb₅: A Z₂ topological kagome metal with a superconducting ground state, *Phys. Rev. Lett.* **125**, 247002 (2020).
- [19] B. R. Ortiz, P. M. Sarte, E. M. Kenney, M. J. Graf, S. M. L. Teicher, R. Seshadri, and S. D. Wilson, Superconductivity in the Z₂ kagome metal KV₃Sb₅, *Phys. Rev. Mater.* **5**, 034801 (2021).
- [20] Z. Jiang, Z. Liu, H. Ma, W. Xia, Z. Liu, J. Liu, S. Cho, Y. Yang, J. Ding, J. Liu, Z. Huang, Y. Qiao, J. Shen, W. Jing, X. Liu, J. Liu, Y. Guo, and D. Shen, Flat bands, non-trivial band topology and rotation symmetry breaking in layered kagome-lattice RbTi₃Bi₅, *Nat. Commun.* **14**, 4892 (2023).
- [21] R. M. Fernandes, A. V. Chubukov, and J. Schmalian, What drives nematic order in iron-based superconductors?, *Nat. Phys.* **10**, 97 (2014).
- [22] S.-Y. Yang, Y. Wang, B. R. Ortiz, D. Liu, J. Gayles, E. Derunova, R. Gonzalez-Hernandez, L. Šmejkal, Y. Chen, S. S. P. Parkin, S. D. Wilson, E. S. Toberer, T. McQueen, and M. N. Ali, Giant, unconventional anomalous hall effect in the metallic frustrated magnet candidate, KV₃Sb₅, *Sci. Adv.* **6**, eabb6003 (2020).
- [23] F. H. Yu, T. Wu, Z. Y. Wang, B. Lei, W. Z. Zhuo, J. J. Ying, and X. H. Chen, Concurrence of anomalous hall effect and charge density wave in a superconducting topological kagome metal, *Phys. Rev. B* **104**, L041103 (2021).
- [24] Z. Liang, X. Hou, F. Zhang, W. Ma, P. Wu, Z. Zhang, F. Yu, J.-J. Ying, K. Jiang, L. Shan, Z. Wang, and X.-H. Chen, Three-dimensional charge density wave and surface-dependent vortex-core states in a kagome superconductor CsV₃Sb₅, *Phys. Rev. X* **11**, 031026 (2021).
- [25] H. W. S. Arachchige, W. R. Meier, M. Marshall, T. Mat-suoka, R. Xue, M. A. McGuire, R. P. Hermann, H. Cao, and D. Mandrus, Charge density wave in kagome lattice intermetallic ScV₆Sn₆, *Phys. Rev. Lett.* **129**, 216402 (2022).
- [26] A. Korshunov, H. Hu, D. Subires, Y. Jiang, D. Călugăru, X. Feng, A. Rajapitamahuni, C. Yi, S. Roychowdhury, M. G. Vergniory, J. Strempler, C. Shekhar, E. Vescovo, D. Chernyshov, A. H. Said, A. Bosak, C. Felser, B. A. Bernevig, and S. Blanco-Canosa, Softening of a flat phonon mode in the kagome ScV₆Sn₆, *Nature Communications* **14**, 6646 (2023).
- [27] S. Cao, C. Xu, H. Fukui, T. Manjo, Y. Dong, M. Shi, Y. Liu, C. Cao, and Y. Song, Competing charge-density wave instabilities in the kagome metal ScV₆Sn₆, *Nature Communications* **14**, 7671 (2023).
- [28] M. Tuniz, A. Consiglio, D. Puntel, C. Bigi, S. Enzner, G. Pokharel, P. Orgiani, W. Bronsch, F. Parmigiani, V. Polewczyk, P. D. C. King, J. W. Wells, I. Zeljkovic, P. Carrara, G. Rossi, J. Fujii, I. Vobornik, S. D. Wilson, R. Thomale, T. Wehling, G. Sangiovanni, G. Panaccione, F. Cilento, D. Di Sante, and F. Mazzola, Dynamics and resilience of the unconventional charge density wave in ScV₆Sn₆ bilayer kagome metal, *Commun. Mater.* **4**, 103 (2023).
- [29] H. Tan and B. Yan, Abundant lattice instability in kagome metal ScV₆Sn₆, *Phys. Rev. Lett.* **130**, 266402 (2023).
- [30] Y.-X. Jiang, S. Shao, W. Xia, M. M. Denner, J. Ingham, M. S. Hossain, Q. Qiu, X. Zheng, H. Chen, Z.-J. Cheng, X. P. Yang, B. Kim, J.-X. Yin, S. Zhang, M. Litskevich, Q. Zhang, T. A. Cochran, Y. Peng, G. Chang, Y. Guo, R. Thomale, T. Neupert, and M. Z. Hasan, Van hove annihilation and nematic instability on a kagome lattice, *Nat. Mater.* **23**, 1214 (2024).
- [31] S. X. M. Riberolles, T. J. Slade, D. L. Abernathy, G. E. Granroth, B. Li, Y. Lee, P. C. Canfield, B. G. Ueland, L. Ke, and R. J. McQueeney, Low-temperature competing magnetic energy scales in the topological ferrimagnet TbMn₆Sn₆, *Phys. Rev. X* **12**, 021043 (2022).
- [32] X. Zhang, Z. Liu, Q. Cui, Q. Guo, N. Wang, L. Shi, H. Zhang, W. Wang, X. Dong, J. Sun, Z. Dun, and J. Cheng, Electronic and magnetic properties of intermetallic kagome magnets RV₆Sn₆ (R=Tb-Tm), *Phys. Rev. Mater.* **6**, 105001 (2022).
- [33] J.-X. Yin, W. Ma, T. A. Cochran, X. Xu, S. S. Zhang, H.-J. Tien, N. Shumiya, G. Cheng, K. Jiang, B. Lian, Z. Song, G. Chang, I. Belopolski, D. Multer, M. Litskevich, Z.-J. Cheng, X. P. Yang, B. Swidler, H. Zhou, H. Lin, T. Neupert, Z. Wang, N. Yao, T.-R. Chang, S. Jia, and M. Zahid Hasan, Quantum-limit chern topological magnetism in TbMn₆Sn₆, *Nature* **583**, 533 (2020).
- [34] M. Li, Q. Wang, G. Wang, Z. Yuan, W. Song, R. Lou, Z. Liu, Y. Huang, Z. Liu, H. Lei, Z. Yin, and S. Wang, Dirac cone, flat band and saddle point in kagome magnet YMn₆Sn₆, *Nat. Commun.* **12**, 3129 (2021).
- [35] M. Shi, F. Yu, Y. Yang, F. Meng, B. Lei, Y. Luo, Z. Sun, J. He, R. Wang, Z. Jiang, Z. Liu, D. Shen, T. Wu, Z. Wang, Z. Xiang, J. Ying, and X. Chen, A new class of bilayer kagome lattice compounds with dirac nodal lines and pressure-induced superconductivity, *Nature Communications* **13**, 2773 (2022).
- [36] D. Werhahn, B. R. Ortiz, A. K. Hay, S. D. Wilson, R. Seshadri, and D. Johrendt, The kagomé metals RbTi₃Bi₅ and CsTi₃Bi₅, *Zeitschrift für Naturforschung B* **77**, 757 (2022).
- [37] X. Chen, X. Liu, W. Xia, X. Mi, L. Zhong, K. Yang, L. Zhang, Y. Gan, Y. Liu, G. Wang, A. Wang, Y. Chai, J. Shen, X. Yang, Y. Guo, and M. He, Electrical and thermal transport properties of the kagome metals ATi₃Bi₅ (A = Rb, Cs), *Phys. Rev. B* **107**, 174510 (2023).
- [38] J. Yang, X. Yi, Z. Zhao, Y. Xie, T. Miao, H. Luo, H. Chen, B. Liang, W. Zhu, Y. Ye, J.-Y. You, B. Gu, S. Zhang, F. Zhang, F. Yang, Z. Wang, Q. Peng, H. Mao, G. Liu, Z. Xu, H. Chen, H. Yang, G. Su, H. Gao, L. Zhao, and X. J. Zhou, Observation of flat band, dirac nodal lines and topological surface states in kagome superconductor CsTi₃Bi₅, *Nat. Commun.* **14**, 4089 (2023).
- [39] H. Li, S. Cheng, B. R. Ortiz, H. Tan, D. Werhahn, K. Zeng, D. Johrendt, B. Yan, Z. Wang, S. D. Wilson, and I. Zeljkovic, Electronic nematicity without charge density waves in titanium-based kagome metal, *Nat. Phys.* **19**, 1591 (2023).
- [40] Y. Hu, C. Le, Y. Zhang, Z. Zhao, J. Liu, J. Ma, N. C. Plumb, M. Radovic, H. Chen, A. P. Schnyder, X. Wu, X. Dong, J. Hu, H. Yang, H.-J. Gao, and M. Shi, Non-trivial band topology and orbital-selective electronic nematicity in a titanium-based kagome superconductor, *Nat. Phys.* **19**, 1827 (2023).
- [41] H. Yang, Y. Ye, Z. Zhao, J. Liu, X.-W. Yi, Y. Zhang, H. Xiao, J. Shi, J.-Y. You, Z. Huang, B. Wang, J. Wang, H. Guo, X. Lin, C. Shen, W. Zhou, H. Chen, X. Dong, G. Su, Z. Wang, and H.-J. Gao, Superconductivity and nematic order in a new titanium-based kagome metal CsTi₃Bi₅ without charge density wave order, *Nat. Commun.* **15**, 9626 (2024).

- [42] B. Liu, M.-Q. Kuang, Y. Luo, Y. Li, C. Hu, J. Liu, Q. Xiao, X. Zheng, L. Huai, S. Peng, Z. Wei, J. Shen, B. Wang, Y. Miao, X. Sun, Z. Ou, S. Cui, Z. Sun, M. Hashimoto, D. Lu, C. Jozwiak, A. Bostwick, E. Rotenberg, L. Moreschini, A. Lanzara, Y. Wang, Y. Peng, Y. Yao, Z. Wang, and J. He, Tunable van hove singularity without structural instability in kagome metal CsTi_3Bi_5 , *Phys. Rev. Lett.* **131**, 026701 (2023).
- [43] H. Yang, Z. Zhao, X.-W. Yi, J. Liu, J.-Y. You, Y. Zhang, H. Guo, X. Lin, C. Shen, H. Chen, X. Dong, G. Su, and H.-J. Gao, Titanium-based kagome superconductor CsTi_3Bi_5 and topological states (2022), [arXiv:2209.03840](https://arxiv.org/abs/2209.03840) [[cond-mat.supr-con](https://arxiv.org/abs/2209.03840)].
- [44] X.-W. Yi, Z.-W. Liao, J.-Y. You, B. Gu, and G. Su, Superconducting, topological, and transport properties of kagome metals CsTi_3Bi_5 and RbTi_3Bi_5 , *Research* **6**, 0238 (2023).
- [45] J. Y. Nie, X. F. Yang, X. Zhang, X. Q. Liu, W. Xia, D. Z. Dai, C. C. Zhao, C. P. Tu, X. M. Kong, X. B. Jin, Y. F. Guo, and S. Y. Li, Pressure-induced double-dome superconductivity in kagome metal CsTi_3Bi_5 (2023), [arXiv:2308.10129](https://arxiv.org/abs/2308.10129) [[cond-mat.supr-con](https://arxiv.org/abs/2308.10129)].
- [46] X.-W. Yi, X.-Y. Ma, Z. Zhang, Z.-W. Liao, J.-Y. You, and G. Su, Large kagome family candidates with topological superconductivity and charge density waves, *Phys. Rev. B* **106**, L220505 (2022).
- [47] E. P. Rosenthal, E. F. Andrade, C. J. Arguello, R. M. Fernandes, L. Y. Xing, X. C. Wang, C. Q. Jin, A. J. Millis, and A. N. Pasupathy, Visualization of electron nematicity and unidirectional antiferroic fluctuations at high temperatures in NaFeAs , *Nat. Phys.* **10**, 225 (2014).
- [48] H. Zhao, H. Li, L. Dong, B. Xu, J. Schneeloch, R. Zhong, M. Fang, G. Gu, J. Harter, S. D. Wilson, Z. Wang, and I. Zeljkovic, Nematic transition and nanoscale suppression of superconductivity in $\text{Fe}(\text{Te},\text{Se})$, *Nat. Phys.* **17**, 903 (2021).
- [49] P. Hohenberg and W. Kohn, Inhomogeneous electron gas, *Phys. Rev.* **136**, B864 (1964).
- [50] P. E. Blöchl, Projector augmented-wave method, *Phys. Rev. B* **50**, 17953 (1994).
- [51] G. Kresse and J. Furthmüller, Efficient iterative schemes for ab initio total-energy calculations using a plane-wave basis set, *Phys. Rev. B* **54**, 11169 (1996).
- [52] G. Kresse and D. Joubert, From ultrasoft pseudopotentials to the projector augmented-wave method, *Phys. Rev. B* **59**, 1758 (1999).
- [53] J. P. Perdew, K. Burke, and M. Ernzerhof, Generalized gradient approximation made simple, *Phys. Rev. Lett.* **77**, 3865 (1996).
- [54] A. A. Mostofi, J. R. Yates, G. Pizzi, Y.-S. Lee, I. Souza, D. Vanderbilt, and N. Marzari, An updated version of wannier90: A tool for obtaining maximally-localised wannier functions, *Comput. Phys. Commun.* **185**, 2309 (2014).
- [55] P. Giannozzi, O. Andreussi, T. Brumme, O. Bunau, M. B. Nardelli, M. Calandra, R. Car, C. Cavazzoni, D. Ceresoli, M. Cococcioni, N. Colonna, I. Carnimeo, A. D. Corso, S. de Gironcoli, P. Delugas, R. A. DiStasio, A. Ferretti, A. Floris, G. Fratesi, G. Fugallo, R. Gebauer, U. Gerstmann, F. Giustino, T. Gorni, J. Jia, M. Kawamura, H.-Y. Ko, A. Kokalj, E. Küçükbenli, M. Lazzeri, M. Marsili, N. Marzari, F. Mauri, N. L. Nguyen, H.-V. Nguyen, A. O. de-la Roza, L. Paulatto, S. Poncé, D. Rocca, R. Sabatini, B. Santra, M. Schlipf, A. P. Seitsonen, A. Smogunov, I. Timrov, T. Thonhauser, P. Umari, N. Vast, X. Wu, and S. Baroni, Advanced capabilities for materials modelling with quantum espresso, *J. Phys.: Condens. Matter* **29**, 465901 (2017).
- [56] S. Poncé, E. Margine, C. Verdi, and F. Giustino, Epw: Electron-phonon coupling, transport and superconducting properties using maximally localized wannier functions, *Comput. Phys. Commun.* **209**, 116 (2016).
- [57] M. van Setten, M. Giantomassi, E. Bousquet, M. Verstraete, D. Hamann, X. Gonze, and G.-M. Rignanese, The pseudodojo: Training and grading a 85 element optimized norm-conserving pseudopotential table, *Comput. Phys. Commun.* **226**, 39 (2018).
- [58] See Supplemental Materials at [URL WILL BE INSERTED BY PUBLISHERS] for converge tests, sublattice-resolved susceptibility, and doping dependent electronic structure of CsTi_3Bi_5 .
- [59] S. Okamoto, N. Mohanta, E. Dagotto, and D. N. Sheng, Topological flat bands in a kagome lattice multiorbital system, *Commun. Phys.* **5**, 198 (2022).
- [60] L. Fu and C. L. Kane, Topological insulators with inversion symmetry, *Phys. Rev. B* **76**, 045302 (2007).
- [61] M. L. Kiesel and R. Thomale, Sublattice interference in the kagome hubbard model, *Phys. Rev. B* **86**, 121105 (2012).
- [62] N. F. Q. Yuan, H. Isobe, and L. Fu, Magic of high-order van hove singularity, *Nature Communications* **10**, 5769 (2019).
- [63] Y.-M. Wu, R. Thomale, and S. Raghu, Sublattice interference promotes pair density wave order in kagome metals, *Phys. Rev. B* **108**, L081117 (2023).
- [64] X. Han, A. P. Schnyder, and X. Wu, Enhanced nematicity emerging from higher-order van hove singularities, *Phys. Rev. B* **107**, 184504 (2023).
- [65] X. Wu, T. Schwemmer, T. Müller, A. Consiglio, G. Sangiovanni, D. Di Sante, Y. Iqbal, W. Hanke, A. P. Schnyder, M. M. Denner, M. H. Fischer, T. Neupert, and R. Thomale, Nature of unconventional pairing in the kagome superconductors AV_3Sb_5 ($\text{A}=\text{K}, \text{Rb}, \text{Cs}$), *Phys. Rev. Lett.* **127**, 177001 (2021).
- [66] Y. Hu, X. Wu, B. R. Ortiz, S. Ju, X. Han, J. Ma, N. C. Plumb, M. Radovic, R. Thomale, S. D. Wilson, A. P. Schnyder, and M. Shi, Rich nature of van hove singularities in kagome superconductor CsV_3Sb_5 , *Nat. Commun.* **13**, 2220 (2022).
- [67] R. S. Markiewicz, B. Singh, C. Lane, and A. Bansil, Investigating the cuprates as a platform for high-order van hove singularities and flat-band physics, *Commun. Phys.* **6**, 292 (2023).
- [68] H. Tan and B. Yan, Competing lattice instability and magnetism on the surface of kagome metals, *Phys. Rev. B* **109**, 195428 (2024).
- [69] P. B. Allen and R. C. Dynes, Transition temperature of strong-coupled superconductors reanalyzed, *Phys. Rev. B* **12**, 905 (1975).